SCIENCE CHINA
Physics, Mechanics & Astronomy

•Article•

September 2023 Vol. 66 No. 9: 297311
https://doi.org/10.1007/s11433-023-2143-2

High-performance violet phosphorus photodetectors with van der Waals-assisted contacts

Hao Wang[1,6†], Shuling Liu[2†], Peng Wang[1,6*], Haonan Ge[1], Yue Chen[1], Hailu Wang[1], Tengfei Xu[4], Jiaxiang Guo[1], Yuanchen Zou[5], Wenrui Wei[1], Ruiqi Jiang[1], Fang Wang[1], Piotr Martyniuk[3], Jinshui Miao[1,6*], and Weida Hu[1,6]

[1] *State Key Laboratory of Infrared Physics, Shanghai Institute of Technical Physics, Chinese Academy of Sciences, Shanghai 200083, China;*
[2] *School of Physics and Photoelectric Engineering, Hangzhou Institute for Advanced Study, University of Chinese Academy of Sciences, Hangzhou 310024, China;*
[3] *Institute of Applied Physics, Military University of Technology, Warsaw 00-908, Poland;*
[4] *Frontier Institute of Chip and System, Fudan University, Shanghai 200438, China;*
[5] *School of Microelectronics, Shanghai University, Shanghai 201800, China;*
[6] *University of Chinese Academy of Sciences, Beijing 100049, China*

Received April 8, 2023; accepted May 15, 2023; published online August 14, 2023

Black phosphorus (BP) as a narrow-bandgap two-dimensional semiconductor material has been extensively studied. And the allotrope violet phosphorus (VP) exhibits wide bandgap properties extending the application in the visible light band. However, due to the Schottky barrier of metal/semiconductor contacts (M/S), further device application of VP is limited. Here, VP-based photodetectors with van der Waals-assisted contact were demonstrated, achieving quasi-Ohmic M/S contacts. The output characteristics in dark conditions show ultralow current at the pA level. And the device exhibits a high current on-off ratio of 10^5 and a fast response speed of 8.4 ms. Furthermore, we constructed the first allotropic photodetector based on BP and VP heterojunction. The device maintains ultralow dark current (~ pA) while exhibiting faster carrier transport, with 945 μs response time and polarization detection capability. These results offer an effective way to study the optoelectronic properties of VP and promote the study of allotropic heterojunction devices.

violet phosphorus, two-dimensional materials, photodetectors, Ohmic contact, allotropic heterojunction

PACS number(s): 73.40.Lq, 73.61.Cw, 73.50.Pz

Citation: H. Wang, S. Liu, P. Wang, H. Ge, Y. Chen, H. Wang, T. Xu, J. Guo, Y. Zou, W. Wei, R. Jiang, F. Wang, P. Martyniuk, J. Miao, and W. Hu, High-performance violet phosphorus photodetectors with van der Waals-assisted contacts, Sci. China-Phys. Mech. Astron. **66**, 297311 (2023), https://doi.org/10.1007/s11433-023-2143-2

1 Introduction

With the discovery of graphene, two-dimensional (2D) materials have been studied extensively. The 2D materials have an atomic-level thickness, and their carrier migration and heat diffusion are all within the two-dimensional scale. Graphene has ultrahigh carrier mobility, but the zero bandgap limits its potential for optoelectronic applications. Black phosphorus (BP) has many advantages such as adjustable narrow bandgap characteristics (~0.34 eV to ~2 eV), wide absorption range, high quantum efficiency, and considerable mobility. However, it is unstable in atmospheric environ-

*Corresponding authors (Peng Wang, email: w_peng@mail.sitp.ac.cn; Jinshui Miao, email: jsmiao@mail.sitp.ac.cn)
†These authors contributed equally to this work.

© Science China Press 2023

ments, limiting its application potential [1-4].

Violet phosphorus (VP) is another 2D material, an allotrope of BP. Zhang et al. [5,6] first reported that the VP was exfoliated by mechanical and liquid methods under ambient conditions. It exhibits better atmospheric stability than BP, having more potential for practical application. The theory predicts that VP has a tunable bandgap characteristic of 2.02-1.69 eV with changing thickness [7]. Compared with the narrow bandgap material BP, it shows application prospects in visible light detection. However, in the existing reports, VP exhibits high contact resistance and Schottky contact properties, which significantly restricts the device performance and further research of VP [8,9].

The contact between the metal and the 2D materials significantly determines the device's performance. To achieve high-performance photoconductors and transistor devices, the establishment of Ohmic contact is essential. Since 2D materials consist solely of surfaces, surface states can readily induce the Fermi-level pinning effect. Due to the complex crystal structure and weak interlayer bonding, there are apparent Schottky barriers (SHB) and the Fermi-level pinning effect between VP and metals, greatly restricting device performance. The possible methods to solve the contact problem include: (1) Transfer the 2D materials to the pre-prepared electrode, which can reduce the interaction between the metal electrode and the 2D materials and improve the quality of the contact layer [10]. (2) Add a buffer layer between the 2D materials and the electrode, reducing the interaction between the metal electrode and the 2D materials [11,12]. (3) Doping the 2D semiconductor materials at contact can significantly reduce contact resistance [13,14]. However, the above methods all have relatively large complexity and difficulty in operability.

In this work, we report VP-based photodetectors with van der Waals-assisted contacts. The device has quasi-Ohmic contact characteristics, achieving a high current switching ratio of 10^5 and 8.4 ms response time which is the fastest in the existing VP optoelectronic device research [15]. Furthermore, we constructed the first allotropic photodetector based on BP and VP heterojunction with van der Waals-assisted contacts. Adopting an Au/graphene/VP/BP vertical stack structure, the device exhibits faster carrier transport speed while maintaining ultra-low dark current (~ pA), with a response time of 945 μs and polarization detection capability.

2 Methods

2.1 VP-graphene photoconductive detector

Mechanical stripping and transfer of 2D materials were performed in a nitrogen glove box. The thicknesses of VP and graphene were about 35 and 8 nm, respectively. Then electron beam lithography (EBL) was used to expose metal electrode patterns on graphene, and Cr/Au (8/50 nm) was evaporated by thermal evaporation coating technology. The whole device is then annealed in a nitrogen atmosphere at 200°C for 1 h. Before device testing, a layer of PMMA can be spin-coated on the device surface as a protective layer to prevent the influence of the atmospheric environment during testing.

2.2 Au/graphene/VP/BP photovoltaic detector

First, the Au bottom electrode was patterned on the Si/SiO_2 (285 nm) substrate by EBL, and then a 15 nm Au film was prepared by thermal evaporation. Then the graphene was mechanically peeled off onto the Au substrate, and VP and BP were sequentially transferred and stacked on top of the graphene using PDMS transfer technology. The above operations were all completed in the glove box. Then use EBL to pattern the top metal electrode. And thermal evaporation coating technology evaporates Cr/Au (8/50 nm) metal electrodes. Then covering the whole surface of the device with h-BN can protect the device. Finally, the whole device was placed in a vacuum annealing furnace for 1 h annealing at 200°C.

2.3 Electrical and optoelectronic measurements

The photoelectric response and photocurrent mapping tests are carried out through the self-built confocal micro-nano photocurrent microscopy characterization system with Keithley 6482 picoammeter. The PicoScope4262 acquires waveform and response time data. Both Raman spectroscopy and photoluminescence (PL) spectral imaging tests were performed by HORIBA LabRam HR800, which was excited by a 532 nm laser. And the atomic force microscope (AFM) and kelvin probe force microscopy (KPFM) tests are based on Oxford's Asylum Research MFP-3D for characterization.

3 Results

3.1 VP-based photoconductive device

The atomic layer structure of the monoclinic VP crystal, illustrated in Figure 1(a), can be observed as a composition of 2D layers containing folded six-membered rings of phosphorus atoms. Each ring in a layer shares an edge with two neighboring rings within the same layer. Weak van der Waals forces hold the layers together. The VP exhibits a complex crystal structure, unlike the BP, a relatively simple orthorhombic structure [16]. Figure 1(b) shows the Raman characteristic of VP. There are more characteristic peaks in the Raman spectrum, which represent a higher phonon density of states [17]. The high-frequency part above 350 cm^{-1} and the low-frequency part below 290 cm^{-1} re-

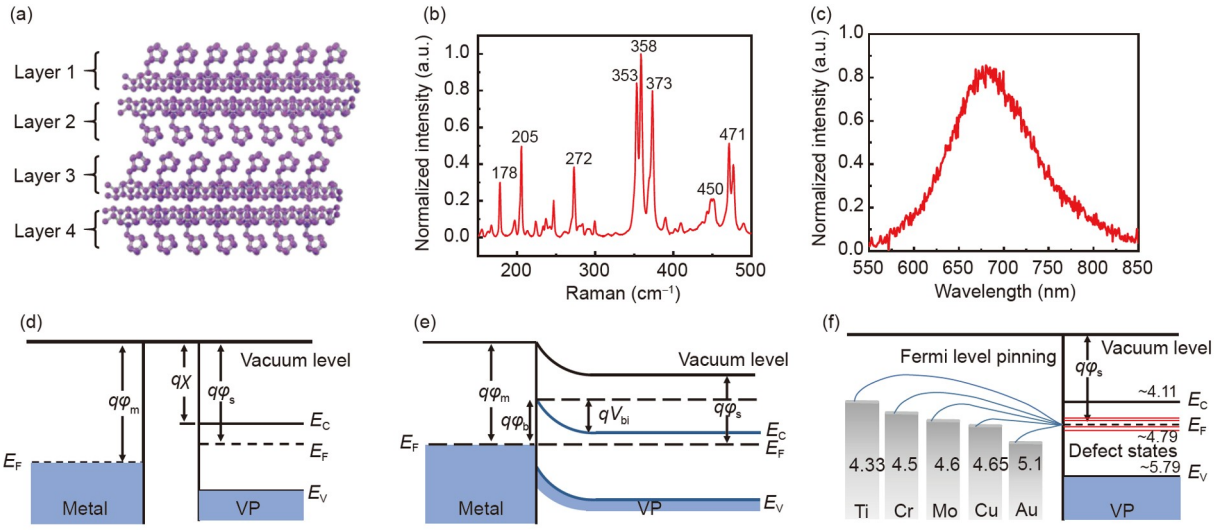


Figure 1 (Color online) Layered structure, spectral characterization of VP, and band alignment at the interface between VP and metals. (a) Layered structure of VP. (b) Normalized Raman spectrum of VP on SiO_2/Si. (c) Normalized PL spectrum of exfoliated VP bulk. (d) The energy band diagram of the metal and VP before equilibrium. (e) The energy band diagram of the metal and VP after equilibrium, ideally. (f) The energy band diagram of various metals and VP under the influence of Fermi-level pinning.

present the main Raman characteristics of VP [18]. The signal's component comes from the lattice structure's stretching and bending, and the low-frequency part comes from bond angle distortion and interlayer van der Waals force. Figure 1(c) is the photoluminescence spectrum of the VP under the 532 nm laser excitation, with a maximum intensity at 680 nm. It represents the exciton recombination process inside VP. Due to the ultra-thin thickness of 2D materials, the Coulomb shielding potential is weak, and the exciton binding energy is large [19,20].

The determination of an Ohmic contact formation relies heavily on the barrier height between the metal and VP. As shown in Figure 1(d) and (e), the barrier height equals the difference between the metal's work function and the semiconductor's electron affinity. Therefore, it is generally necessary to select a metal that matches the work function of the VP for good contact [21]. However, the interface's defects and work function differences determine the potential barrier between metals and 2D materials. If the material has many defect levels, it will cause a strong Fermi-level pinning effect [22,23]. Since 2D materials have only two dimensions in a plane, electrons can only move within a limited range of energy levels and are easily confined to areas with lower energy levels, resulting in discontinuous electron density distribution. In particular, the process of preparing materials and metal electrodes also introduces many defect levels. These will lead to the existence of the Fermi pinning effect in 2D materials, resulting in the SHB hardly changing with the change of the work function [24]. In addition, 2D materials with intricate structures can exhibit numerous lattice defects, including point defects, line defects, and planar defects, among others. These defects lead to non-uniformity of energy levels, introducing defect energy levels [25]. As mentioned above, the VP has a complex tubular lattice structure and the van der Waals force between layers is feeble, easily leading to the generation of defect levels. Figure 1(f) shows the comparison of work functions with VP and several metals [26,27]. These metals have similar work functions and are theoretically the most promising metals to form an excellent quasi-Ohmic contact with VP. We fabricated photodiode devices based on all the metals shown in Figure 1(d). But all these VP devices with metal electrodes have apparent Schottky contact characteristics, as shown in Figure 2(e).

Due to their similar 2D layered structure, graphene and VP exhibit a weak interaction at their interface, resulting in a reduced Fermi-level pinning effect. Consequently, the barrier height can be effectively modulated, achieving quasi-Ohmic contact between the two materials. This remarkable feature offers excellent potential for developing advanced electronic and optoelectronic devices, where efficient charge injection and transport across the interface are crucial [28,29]. As shown in Figure 2(a), we fabricated a VP-based photodetector with graphene electrodes. Figure S1 (in Supporting Information) shows the measurement of the thicknesses of graphene and VP by AFM as 8 and 36 nm, respectively. The graphene was subsequently connected to Cr/Au (8/50 nm) electrodes. To enhance the quality of the interface layer in the device, an annealing treatment was conducted at a temperature of 200°C for a duration of 1 h. Additionally, cross-sectional transmission electron microscopy (TEM) measurements of the VP-graphene interface was conducted to further verify the contact quality, as illustrated in Figure 2(b). A 2 nm oxide layer exists between VP and graphene, which may be due to the movement in the atmosphere or introduced

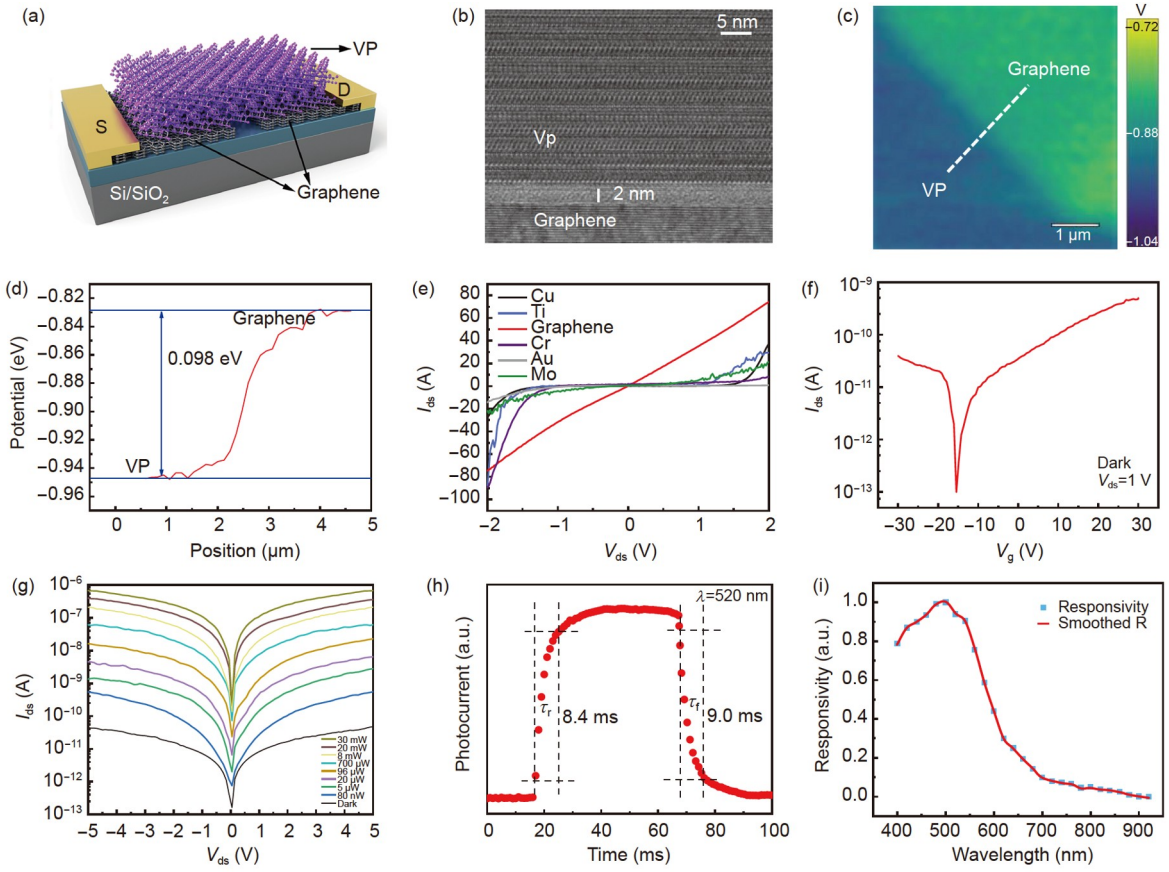


Figure 2 (Color online) VP photoconductive photodetector contacted by graphene symmetric electrodes. (a) The schematic of VP photodetectors structure contacted by graphene symmetric electrodes. (b) TEM image at the interface of the VP/graphene structure. (c) KPFM image of VP and graphene flakes. (d) Contact potential difference between VP and graphene flakes. (e) Output characteristic curves of the VP-based photodetector device at different metals or graphene electrode contacts. (f) Transfer characteristic curve of the device with V_{ds}=1 V. (g) Output characteristic curves of the device under 520 nm laser illumination with increasing powers. (h) Response time of the device under 520 nm illumination at V_{ds} = 2 V. The corresponding τ_r and τ_f are 8.4 and 9 ms, respectively. (i) Photoresponse spectrum of the device under the laser illumination with the wavelength from 400 to 920 nm.

during TEM sample preparation and testing. During annealing, the environment is non-pure nitrogen gas, and a small amount of oxygen may still mix in, which may also be a reason for the presence of the oxide layer. Previous studies have also frequently reported the oxide layer between two-dimensional material layers [30,31]. The ultra-thin dielectric layer, as a natural tunneling barrier, does not significantly affect the carrier transport and helps to weaken the Fermi level pinning effect at the interface of the two-dimensional materials. In order to precisely ascertain the junction barrier at the VP-graphene interface, the surface potential of both VP and multilayer graphene was measured by KPFM, as depicted in Figure 2(c) and (d). The surface potential of multilayer graphene is higher than that of VP, indicating a lower work function for VP. The surface potential of multilayer graphene is higher than that of VP, indicating a lower work function for VP. The Fermi level difference between VP and multilayer graphene contacts is only 98 meV, contributing to good electrical contact. As shown in Figure 2(e), it is clear that the performance of the graphene-based device surpasses other devices with metal electrodes. The I_{ds}-V_{ds} curve in the dark state is close to a linear change, realizing a quasi-Ohmic contact [32]. While the barrier of the contact layer is reduced, the device has an ultralow dark current of pA level with an on-off ratio exceeding 10^5 as shown in Figure S2(a). And Figure S2(b) shows changes with the optical power of the responsivity. As the incident optical power increases, the responsivity gradually decreases. When the optical power is 9 nW, the responsivity of the device is about 4.2 mA/W. When the optical power is 8 mW, the response rate of the device is about 0.07 mA/W. The changing trend begins to stabilize and gradually approaches saturation. Figure 2(f) shows the transfer characteristic curve at 1 V bias, which exhibits n-type characteristics and may be caused by the doping effect introduced during the material preparation process. The output characteristic curves of the VP-graphene-based device are shown in Figure 2(g) under different powers of a 520 nm laser. As the optical power increases, the photocurrent increases slowly and approaches saturation. Each characteristic output curve exhibits good symmetry, reflecting good quasi-Ohmic contacts. The scanning photocurrent microscopy mapping was tested with 2 V

bias at 300 K under 520 nm laser illumination with a power density of 15.5 mW cm^{-2}, shown in Figure S3. And the spatial distribution of the photoresponse is mainly concentrated in the VP region. Figure S4 is the schematic diagram of the band alignment of VP and graphene before equilibrium and under biased and lighting conditions. The almost non-existent Schottky barrier effectively facilitates the transport of photogenerated electron-hole pairs. As shown in Figure 2(h), the device has good response time performance: the rise and decay processes are fast, with a rise time (τ_r) of 8.4 ms and a fall time (τ_f) of 9 ms, which are among the fastest response time for VP-based photodetectors. The fast response is attributed to the bilateral graphene electrode contact design. Due to the extremely low contact barrier, the photogenerated carriers can pass through the interface smoothly and effectively, and the effects of defect recombination and Fermi-level pinning are significantly reduced. Figure 2(i) shows the photocurrent response characteristics of the device in the visible light band. There is a strong photoresponse between 400-650 nm, derived from the broad bandgap characteristics of VP and consistent with the PL spectral characteristics of VP.

3.2 VP/BP-based photovoltaic device

The BP, a narrow bandgap semiconductor material, has been widely studied in optoelectronic devices [33-35]. The BP and VP belong to allotropes, and their distinct crystal and band structures offer the possibility to form unique elementary van der Waals heterojunctions. We fabricated the BP/VP heterojunction photodetector for the first time. Figure 3(a) shows a schematic diagram of the Au/graphene/VP/BP vertical stack structure of the device. The Raman spectral properties of the heterojunction were characterized under excitation with a 532 nm laser, shown in Figure S5. The Raman spectrum of BP has three distinct peaks at wavenumbers 362, 440, and 466 cm^{-1}, corresponding to the A_g^1, E_{2g}, and A_g^2 Raman vibrational modes [36]. As mentioned above, the Raman spectrum of the VP region shows its characteristic peaks in both the low-frequency region less than 274 cm^{-1} and the high-frequency region higher than 354 cm^{-1}. The Raman spectrum of the heterojunction region has both the Raman characteristic peaks of BP and VP. To further characterize the interface quality between materials, a cross-sectional TEM measurement of graphene/VP/BP structure was performed, shown in Figure S6. The TEM images reveal a natural vdW heterostructure with only a 2.4 nm oxide gap between VP, BP, and graphene. An excellent interface with van der Waals-assisted contact can avoid the influence of defect states on carrier transport. Then the thicknesses of BP and VP were acquired by AFM, shown in Figure S7, with the thicknesses of BP and VP being 32 and 84 nm, respectively. The output characteristic curves of the device in the dark state and under light are shown in Figure 3(b). Under illumination, it shows an apparent open circuit voltage of 0.21 V and a short circuit current of 61 pA, which

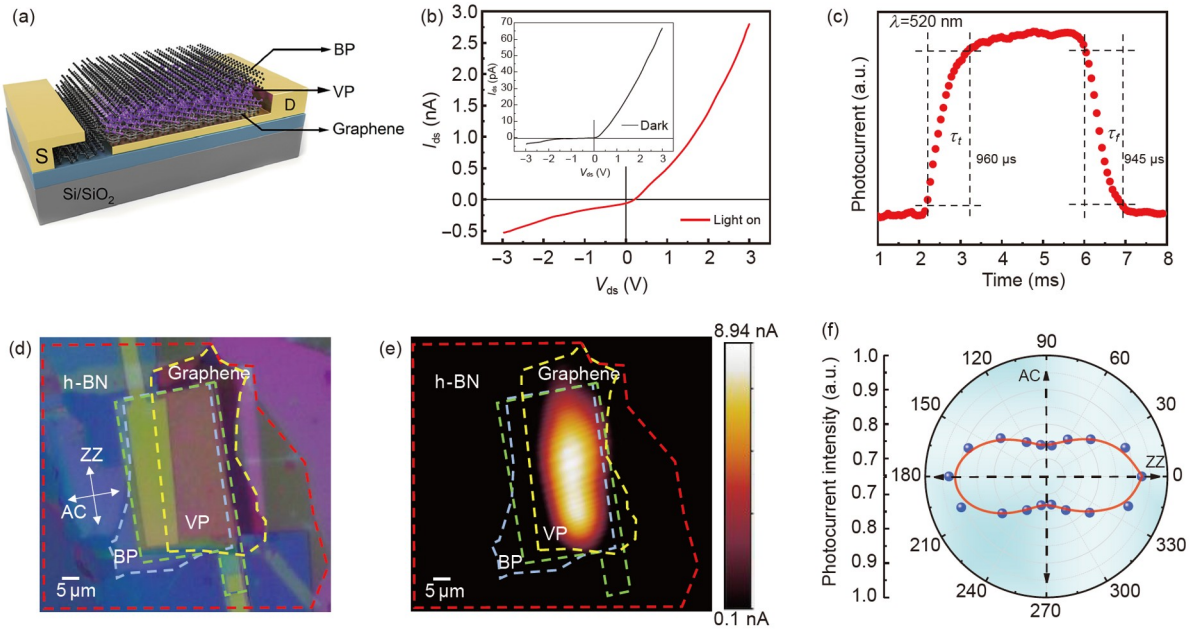


Figure 3 (Color online) BP-VP-based photovoltaic device with van der Waals-assisted contact. (a) The schematic of BP-VP-based photovoltaic device structure. (b) Output characteristic curve of the device under 520 nm laser illumination at zero bias. Inset: the corresponding output characteristic curve under the dark condition at zero bias. (c) Response time of the device under 520 nm illumination at a V_{ds} = 0 V. The corresponding τ_{rise} and τ_{down} are 960 and 945 μs, respectively. (d) Optical photograph of the VP-BP device, h-BN protects the surface. ZZ and AC represent the zigzag and armchair lattice directions of BP, respectively. (e) Photocurrent mapping operating under the illumination of a 520 nm laser. (f) Photocurrent measured at room temperature as a function of incident light polarization angle. ZZ and AC represent the polarization direction of the incident light along the zigzag or armchair lattice direction of BP.

are the characteristics of photovoltaic devices [37]. As a comparison, we prepared VP/BP heterojunction devices with Cr/Au electrodes, which also exhibited photovoltaic response characteristics but showed poorer electrode contact, lower current, and significant fluctuations in both dark and illuminated output characteristics, as shown in Figure S8. We further measured the response speed of the photovoltaic device under 0 V bias by a 520 nm laser, shown in Figure 3(c). The rise time (τ_r = 960 μs) and the decay time (τ_d = 945 μs) are obtained. The response speed is faster than VP-based photoconductive photodetector, which benefits from the vertical structure design and built-in electric field to promote the rapid separation of carriers. An optical photograph and photocurrent mapping image of the device are presented in Figure 3(d) and (e). Since BP is unstable in atmospheric conditions, we used h-BN to passivate the device [38]. The scanning photocurrent microscope mapping was performed under 0 V bias at 300 K, by 520 nm laser with a power density of 20.3 mW cm^{-2}. The strongest response region is obviously concentrated in the overlapping area of BP and VP, indicating that this region forms an effective heterojunction region [39]. The device also exhibits polarization response characteristics under the irradiation of a 520 nm linearly polarized laser, shown in Figure 3(f). The dichroic ratio is calculated using $r = I_{ph(max)}/I_{ph(min)}$ to be 1.27. However, we have not observed effective polarized light response characteristics in VP-based photoconductive photodetectors. We attribute the observed visible polarization response to the optical anisotropy of the BP in the visible region. Compared with the armchair direction, the device exhibits a larger photocurrent response when the incident light polarization direction is along the zigzag direction of BP. The BP exhibits obvious optical anisotropy in the visible band along the armchair and zigzag lattice directions, which also affects the visible light absorption of the underlying VP [40].

The surface potential difference at the VP-BP heterojunction interface was accurately determined based on the KPFM technique, as shown in Figure 4(a) and (b). The surface potential decreases by 0.238 eV from BP to VP region, which means that the work function of VP is smaller than that of BP by about 0.238 eV. Based on the KPFM results, we further simulated the energy band alignment between VP and BP by Sentaurus-TCAD, as shown in Figure 4(c). A type I heterojunction is formed at the interface between VP and BP, and the direction of the built-in electric field is directed from VP to BP [41,42]. To further verify the energy-level matching properties of BP-VP, we performed a PL mapping on the BP-VP heterojunction. As shown in Figure 4(d) and (e), the fluorescence quenching phenomenon of VP was observed in the heterojunction region of BP-VP, indicating that carriers transferred from VP to BP [43]. In Figure 4(f), the black and red PL spectral lines correspond to the black and red marked areas in Figure 4(d), respectively. It can be clearly observed that the PL peak intensity of the pure VP region is stronger than that of the VP-BP heterojunction

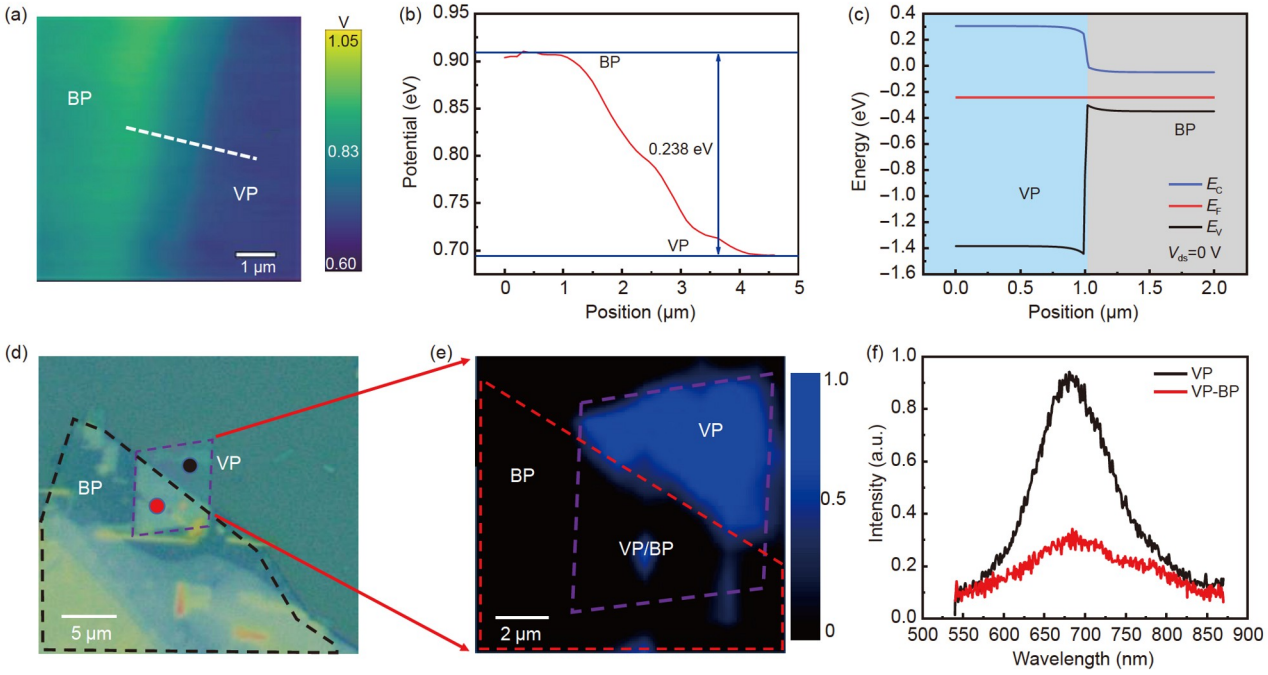


Figure 4 (Color online) Band alignment and PL spectral analysis of BP-VP heterojunction. (a) Surface potential image of the BP-VP heterojunction. (b) Contact potential difference between BP and VP flakes. (c) Simulation diagram of energy band alignment of VP and BP by Sentaurus-TCAD. (d) Optical photography of BP and VP heterojunction and (e) photoluminescence mapping under 520 nm laser excitation. (f) The photoluminescence spectra of VP and BP-VP heterojunction region, corresponding to the areas marked by the black dot and red dot in (d), respectively.

region, and the former is about 3.6 times that of the latter. There is an apparent fluorescence quenching effect in the VP-BP region. In 2D materials heterojunctions, fluorescence quenching occurs due to the energy transfer between one material's excited state and another's electronic state. This further demonstrates VP and BP's type I heterojunction energy band relationship [44-46].

Based on the above discussion, the energy band profiles of BP-VP-graphene before equilibrium and under illumination are obtained, as shown in Figure S9, respectively. Under illumination, the rapid separation of photogenerated electron-hole pairs occurs due to the presence of the built-in electric field. Electrons are efficiently transported to VP, while holes are transported to BP. The large valence band drop from VP to BP facilitates the fast transport of holes. And there is no electron transfer barrier between VP and graphene, which also facilitates the transport of electrons. The type I heterojunction feature makes it difficult for electrons in BP to cross the large conduction band barrier into VP, so we did not detect an effective photoelectric response in the infrared band. But this also reduces the contribution of BP to dark current and contributes to the fact that heterojunction devices can still maintain pA-level dark current [47]. On the other hand, we employed a vertically stacked structure of BP-VP-graphene-Au to achieve large-area electrode contacts at each interface. This vertical device structure shortens the transport distance of carriers and further improves the response speed of the device [30,48].

4 Conclusion

In summary, we demonstrated the VP-based photodetector with van der Waals-assisted contacts, achieving a fast response time of 8.4 ms and a high on-off ratio of 10^5 while maintaining the pA-level dark current. A practical solution to the problem of poor electrical contact in VP phototransistors has been created. Further, the VP/BP elementary phosphorus van der Waals heterojunction photodetector based on the vertical structure achieves a faster response time, shortened to 945 μs, while maintaining the pA-level dark current. The elementary phosphorus van der Waals heterojunction devices are expected to undergo one-time material growth and have excellent industrial application prospects [49,50]. The characteristics of ultra-low dark current at room temperature provide a wide range of applications for VP-based optoelectronic devices in the field of weak signal detection in dark backgrounds and low-power logic devices.

This work was supported by the National Natural Science Foundation of China (Grant Nos. 62261136552, 62005303, and 62134001), the National Key Research and Development Program of China (Grant No. 2021YFA0715602), the International Partnership Program of Chinese Academy of Sciences (Grant No. 181331KYSB20200012), the Shanghai Science and Technology Committee (Grant No. 23YF1455400), and the Open Research Projects of Zhejiang Lab (Grant No. 2022NK0AB01).

Conflict of interest The authors declare that they have no conflict of interest.

Supporting Information

The supporting information is available online at http://phys.scichina.com and https://link.springer.com. The supporting materials are published as submitted, without typesetting or editing. The responsibility for scientific accuracy and content remains entirely with the authors.

1 Y. Chen, Y. Wang, Z. Wang, Y. Gu, Y. Ye, X. Chai, J. Ye, Y. Chen, R. Xie, Y. Zhou, Z. Hu, Q. Li, L. Zhang, F. Wang, P. Wang, J. Miao, J. Wang, X. Chen, W. Lu, P. Zhou, and W. Hu, Nat. Electron. **4**, 357 (2021).
2 G. Abellán, S. Wild, V. Lloret, N. Scheuschner, R. Gillen, U. Mundloch, J. Maultzsch, M. Varela, F. Hauke, and A. Hirsch, J. Am. Chem. Soc. **139**, 10432 (2017).
3 Y. Abate, D. Akinwande, S. Gamage, H. Wang, M. Snure, N. Poudel, and S. B. Cronin, Adv. Mater. **30**, 1704749 (2018).
4 F. Wang, T. Zhang, R. Xie, A. Liu, F. Dai, Y. Chen, T. Xu, H. Wang, Z. Wang, L. Liao, J. Wang, P. Zhou, and W. Hu, Adv. Mater., doi: 10.1002/adma.202301197.
5 L. Zhang, H. Huang, B. Zhang, M. Gu, D. Zhao, X. Zhao, L. Li, J. Zhou, K. Wu, Y. Cheng, and J. Zhang, Angew. Chem. Int. Ed. **59**, 1074 (2020).
6 A. Fali, M. Snure, and Y. Abate, Appl. Phys. Lett. **118**, 163105 (2021).
7 B. Zhang, Z. Wang, H. Huang, L. Zhang, M. Gu, Y. Cheng, K. Wu, J. Zhou, and J. Zhang, J. Mater. Chem. A **8**, 8586 (2020).
8 S. Lin, W. K. Lai, Y. Li, W. Lu, G. Bai, and S. P. Lau, SmartMat **2**, 226 (2021).
9 Y. Li, S. Cai, W. K. Lai, C. Wang, L. Rogée, L. Zhuang, L. Zhai, S. Lin, M. Li, and S. P. Lau, Adv. Opt. Mater. **10**, 2101538 (2021).
10 Y. Liu, J. Guo, E. Zhu, L. Liao, S. J. Lee, M. Ding, I. Shakir, V. Gambin, Y. Huang, and X. Duan, Nature **557**, 696 (2018).
11 M. Lei, S. Fan, Y. Yu, J. Hu, K. Chen, Y. Gu, C. Wu, Y. Zhang, and C. Li, Energy Stor. Mater. **47**, 551 (2022).
12 G. S. Kim, S. H. Kim, J. Park, K. H. Han, J. Kim, and H. Y. Yu, ACS Nano **12**, 6292 (2018).
13 Z. Gao, Z. Zhou, and D. Tománek, ACS Nano **13**, 5103 (2019).
14 K. Hemanjaneyulu, J. Kumar, and M. Shrivastava, IEEE Trans. Electron. Devices **66**, 3224 (2019).
15 A. G. Ricciardulli, Y. Wang, S. Yang, and P. Samorì, J. Am. Chem. Soc. **144**, 3660 (2022).
16 L. Cartz, S. R. Srinivasa, R. J. Riedner, J. D. Jorgensen, and T. G. Worlton, J. Chem. Phys. **71**, 1718 (1979).
17 D. J. Olego, J. A. Baumann, M. A. Kuck, R. Schachter, C. G. Michel, and P. M. Raccah, Solid State Commun. **52**, 311 (1984).
18 L. Zhang, H. Huang, Z. Lv, L. Li, M. Gu, X. Zhao, B. Zhang, Y. Cheng, and J. Zhang, ACS Appl. Electron. Mater. **3**, 1043 (2021).
19 M. M. Ugeda, A. J. Bradley, S. F. Shi, F. H. da Jornada, Y. Zhang, D. Y. Qiu, W. Ruan, S. K. Mo, Z. Hussain, Z. X. Shen, F. Wang, S. G. Louie, and M. F. Crommie, Nat. Mater. **13**, 1091 (2014).
20 F. Cadiz, E. Courtade, C. Robert, G. Wang, Y. Shen, H. Cai, T. Taniguchi, K. Watanabe, H. Carrere, D. Lagarde, M. Manca, T. Amand, P. Renucci, S. Tongay, X. Marie, and B. Urbaszek, Phys. Rev. X **7**, 021026 (2017).
21 M. Moun, and R. Singh, Bull. Mater. Sci. **44**, 223 (2021).
22 X. Liu, M. S. Choi, E. Hwang, W. J. Yoo, and J. Sun, Adv. Mater. **34**, 2108425 (2022).
23 C. Kim, I. Moon, D. Lee, M. S. Choi, F. Ahmed, S. Nam, Y. Cho, H. J. Shin, S. Park, and W. J. Yoo, ACS Nano **11**, 1588 (2017).
24 S. McDonnell, R. Addou, C. Buie, R. M. Wallace, and C. L. Hinkle, ACS Nano **8**, 2880 (2014).

25 Z. Xiong, L. Zhong, H. Wang, and X. Li, Materials **14**, 1192 (2021).
26 G. N. Derry, M. E. Kern, and E. H. Worth, J. Vac. Sci. Technol. A **33**, 060801 (2015).
27 H. B. Michaelson, J. Appl. Phys. **48**, 4729 (1977).
28 Y. Wang, Z. Wan, Q. Qian, Y. Liu, Z. Kang, Z. Fan, P. Wang, Y. Wang, C. Li, C. Jia, Z. Lin, J. Guo, I. Shakir, M. Goorsky, X. Duan, Y. Zhang, Y. Huang, and X. Duan, Nat. Nanotechnol. **15**, 768 (2020).
29 Z. Bian, J. Miao, Y. Zhao, and Y. Chai, Acc. Mater. Res. **3**, 1220 (2022).
30 J. Miao, C. Leblanc, J. Wang, Y. Gu, X. Liu, B. Song, H. Zhang, S. Krylyuk, W. Hu, A. V. Davydov, T. Back, N. Glavin, and D. Jariwala, Nat. Electron. **5**, 744 (2022).
31 H. Jiao, X. Wang, Y. Chen, S. Guo, S. Wu, C. Song, S. Huang, X. Huang, X. Tai, T. Lin, H. Shen, H. Yan, W. Hu, X. Meng, J. Chu, Y. Zhang, and J. Wang, Sci. Adv. **8**, eabn1811 (2022).
32 Y. Zheng, J. Gao, C. Han, and W. Chen, Cell Rep. Phys. Sci. **2**, 100298 (2021).
33 L. Li, Y. Yu, G. J. Ye, Q. Ge, X. Ou, H. Wu, D. Feng, X. H. Chen, and Y. Zhang, Nat. Nanotech. **9**, 372 (2014).
34 Q. Guo, A. Pospischil, M. Bhuiyan, H. Jiang, H. Tian, D. Farmer, B. Deng, C. Li, S. J. Han, H. Wang, Q. Xia, T. P. Ma, T. Mueller, and F. Xia, Nano Lett. **16**, 4648 (2016).
35 S. Yuan, D. Naveh, K. Watanabe, T. Taniguchi, and F. Xia, Nat. Photon. **15**, 601 (2021).
36 H. B. Ribeiro, M. A. Pimenta, and C. J. S. de Matos, J. Raman Spectrosc. **49**, 76 (2018).
37 M. Long, P. Wang, H. Fang, and W. Hu, Adv. Funct. Mater. **29**, 1803807 (2019).
38 J. Zhang, B. Tan, X. Zhang, F. Gao, Y. Hu, L. Wang, X. Duan, Z. Yang, and P. A. Hu, Adv. Mater. **33**, 2000769 (2021).
39 L. Britnell, R. M. Ribeiro, A. Eckmann, R. Jalil, B. D. Belle, A. Mishchenko, Y. J. Kim, R. V. Gorbachev, T. Georgiou, S. V. Morozov, A. N. Grigorenko, A. K. Geim, C. Casiraghi, A. H. C. Neto, and K. S. Novoselov, Science **340**, 1311 (2013).
40 N. Mao, J. Tang, L. Xie, J. Wu, B. Han, J. Lin, S. Deng, W. Ji, H. Xu, K. Liu, L. Tong, and J. Zhang, J. Am. Chem. Soc. **138**, 300 (2016).
41 F. Yan, Z. Wei, X. Wei, Q. Lv, W. Zhu, and K. Wang, Small Methods **2**, 1700349 (2018).
42 F. Wu, Q. Li, P. Wang, H. Xia, Z. Wang, Y. Wang, M. Luo, L. Chen, F. Chen, J. Miao, X. Chen, W. Lu, C. Shan, A. Pan, X. Wu, W. Ren, D. Jariwala, and W. Hu, Nat. Commun. **10**, 4663 (2019).
43 X. Zong, H. Hu, G. Ouyang, J. Wang, R. Shi, L. Zhang, Q. Zeng, C. Zhu, S. Chen, C. Cheng, B. Wang, H. Zhang, Z. Liu, W. Huang, T. Wang, L. Wang, and X. Chen, Light Sci. Appl. **9**, 114 (2020).
44 T. Yamaoka, H. E. Lim, S. Koirala, X. Wang, K. Shinokita, M. Maruyama, S. Okada, Y. Miyauchi, and K. Matsuda, Adv. Funct. Mater. **28**, 1801021 (2018).
45 G. Nayak, S. Lisi, W. L. Liu, T. Jakubczyk, P. Stepanov, F. Donatini, K. Watanabe, T. Taniguchi, A. Bid, J. Kasprzak, M. Richard, V. Bouchiat, J. Coraux, L. Marty, N. Bendiab, and J. Renard, Phys. Rev. Mater. **3**, 114001 (2019).
46 W. Zheng, B. Zheng, Y. Jiang, C. Yan, S. Chen, Y. Liu, X. Sun, C. Zhu, Z. Qi, T. Yang, W. Huang, P. Fan, F. Jiang, X. Wang, X. Zhuang, D. Li, Z. Li, W. Xie, W. Ji, X. Wang, and A. Pan, Nano Lett. **19**, 7217 (2019).
47 Y. Xiao, H. Zhu, K. Deng, P. Wang, Q. Li, T. He, T. Zhang, J. Miao, N. Li, W. Lu, N. Dai, and W. Hu, Sci. China-Phys. Mech. Astron. **65**, 287301 (2022).
48 F. Wang, Z. Liu, T. Zhang, M. Long, X. Wang, R. Xie, H. Ge, H. Wang, J. Hou, Y. Gu, X. Hu, Z. Song, S. Wang, Q. Dong, K. Liao, Y. Tu, T. Han, F. Li, Z. Zhang, X. Hou, S. Wang, L. Li, X. Zhang, D. Zhao, C. Shan, L. Shan, and W. Hu, Adv. Mater. **34**, 2203283 (2022).
49 L. Zhang, M. Gu, L. Li, X. Zhao, C. Fu, T. Liu, X. Xu, Y. Cheng, and J. Zhang, Chem. Mater. **32**, 7363 (2020).
50 Z. Zhang, D. H. Xing, J. Li, and Q. Yan, CrystEngComm **19**, 905 (2017).